

Massive-mode polarization entangled biphoton frequency comb

Tomohiro Yamazaki,¹ Rikizo Ikuta,^{1,2,*} Toshiki Kobayashi,^{1,2} Shigehito Miki,^{3,4}
Fumihiko China,³ Hiroataka Terai,³ Nobuyuki Imoto,² and Takashi Yamamoto^{1,2,†}

¹Graduate School of Engineering Science, Osaka University, Toyonaka, Osaka 560-8531, Japan

²Center for Quantum Information and Quantum Biology,

Institute for Open and Transdisciplinary Research Initiatives, Osaka University, Osaka 560-8531, Japan

³Advanced ICT Research Institute, National Institute of Information
and Communications Technology (NICT), Kobe 651-2492, Japan

⁴Graduate School of Engineering, Kobe University, Kobe 657-0013, Japan

(Dated: December 23, 2024)

Biphoton frequency comb (BFC) having quantum entanglement in a high dimensional system is widely applicable to quantum communication and quantum computation. However, a dozen mode realized so far has not been enough to realize its full potential. Here, we show a massive-mode BFC with polarization entanglement experimentally realized by a nonlinear optical waveguide resonator. The generated BFC at least 1400 modes is broad and dense, that strongly enhances the advantage of BFC. We also demonstrated a versatile property of the present BFC, which enables us to prepare both the frequency-multiplexed entangled photon pair and the high dimensional hyperentangled one. The versatile, stable and highly efficient system with the massive-mode BFC will open up a large-scale photonic quantum information platform.

INTRODUCTION

Entangled photon pairs are essential resources for quantum information processing such as quantum communication [1, 2], quantum computation [3, 4] and quantum metrology [5]. To develop better photon resources, fully utilizing the degrees of freedom (DOF) of photons is a crucial challenge. Recently, quantum nature of frequency DOF of photons is intensively studied [6, 7]. Especially, the quantum frequency comb [8, 9], which is superposition of frequency modes different at a certain mode spacing, is attracting attention because of great advantage to the generation [10–12] and manipulation [13–16] of high dimensional quantum states. A quantum frequency comb formed by a frequency entangled photon pair, which is referred to as biphoton frequency comb (BFC), is a building block of quantum information processing relying on its frequency DOF. Additional entanglement in another DOF of BFC extends use case to various applications as (a) a high dimensional hyperentangled photon pair [15, 17, 18] or (b) a frequency-multiplexed entangled photon pair [19], which have been studied in different contexts.

First, we show a simplified model for generating polarization entangled BFCs (a) and (b) based on spontaneous parametric down conversion (SPDC). Suppose that all frequency modes of BFC are well separated from each other, and complex squeezing parameter ζ is uniform throughout the frequency and polarization modes and proportional to the complex amplitude of the SPDC pump light. Under the assumptions, the quantum state generated by SPDC is written by

$$|\Psi\rangle = \left(\prod_{m=1}^M S_{m,H}(\zeta) S_{m,V}(\zeta) \right) |0\rangle, \quad (1)$$

where $|0\rangle$ represents vacuum state. Here, $S_{m,H(V)}(\zeta) = \exp\left(-\zeta a_{i,m,H(V)}^\dagger a_{s,m,H(V)}^\dagger - h.c.\right)$ is a two-mode squeezing operator where m ($1 \leq m \leq M$) and $H(V)$ represent frequency-mode index and horizontal (vertical) polarization, respectively. In each frequency-index m and $H(V)$ polarization, we define creation operators $a_{s,m,H(V)}^\dagger$ and $a_{i,m,H(V)}^\dagger$ for signal (s) and idler (i) modes. Note that, especially in this paper, s and i indicate distinct frequency modes satisfying the energy conservation via SPDC.

Starting from Eq. (1), we can prepare two different states (a) and (b) by only adjusting the pump power through parameter ζ as follows: (a) In the low pump power regime satisfying $2M|\zeta|^2 \ll 1$, a single photon pair state is represented by

$$|\Psi\rangle \simeq \frac{1}{\sqrt{2}} \left(|HH\rangle_{i,s} + |VV\rangle_{i,s} \right) \otimes \frac{1}{\sqrt{M}} \left(\sum_{m=1}^M |\omega_m \omega_m\rangle_{i,s} \right), \quad (2)$$

where $|\omega_{i(s),m}\rangle$ represents a state of the idler (signal) photon in frequency-index m . This state corresponds to the polarization-frequency hyperentangled state (a), which is valuable for many protocols with hyperentanglement [20–23]. (b) In the case of $2|\zeta|^2 \ll 1$, the generated state in each frequency mode is approximately a single photon pair and represented as

$$|\Psi\rangle \propto \bigotimes_{m=1}^M \left[|0\rangle_m + \zeta \left(|HH\rangle_{i,m,s,m} + |VV\rangle_{i,m,s,m} \right) \right]. \quad (3)$$

This state is equivalent to the state formed by many polarization entangled photon pairs in different frequency indices sharing the single pump light. This frequency-multiplexed entangled photon pair (b) is applicable to high-speed quantum communications [24] and quantum

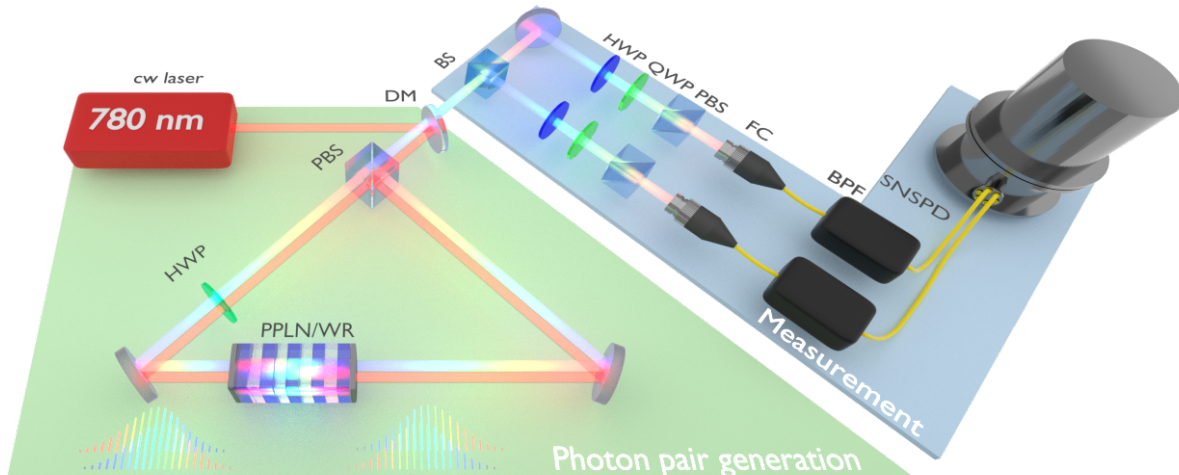


Figure 1: Experimental setup for the generation and measurement of quantum states. BS, beamsplitter; PBS, polarizing beamsplitter; HWP, half-wave plate; QWP, quarter-wave plate; DM, dichroic mirror; FC, fiber coupler; BPF, bandpass filter; SNSPD, superconducting nanowire single photon detector.

communication network [25].

BFCs are efficiently generated by SPDC or spontaneous four-wave mixing (SFWM) inside a cavity. Usually, a photon pair generated by SPDC/SFWM without a cavity has a broad bandwidth determined by the phase-matching condition, but these processes are focused on the resonant frequency modes by cavity confinement of the photons. This results in a highly efficient generation of BFCs. So far, BFCs have mostly been generated by SFWM [7, 10, 19, 26, 27] and SPDC [28, 29] with microring resonators [30]. However, the number of their frequency modes is limited to a dozen. In our experiment, we used a monolithically-integrated periodically-poled LiNbO₃ waveguide resonator (PPLN/WR) which confines only longer-wavelength (signal) photons of the photon pairs and does not confine shorter-wavelength (idler) photons (see Methods). Thanks to the monolithic structure, only the temperature control of the PPLN/WR is enough for stabilization of the cavity. We realize the generation of massive polarization entangled BFC ranging over 1000 modes by placing the singly resonant PPLN/WR into a Sagnac interferometer. In addition to its phase stability [31, 32], the Sagnac interferometer with the single resonator enables us to accomplish a perfect spectral overlap between the H- and V-polarized BFCs.

RESULTS

Figure 1 shows the experimental setup. We use a continuous-wave (cw) pump laser at 780.24 nm whose

power is adjustable from 50 μW to 5 mW (see Methods). The Sagnac interferometer consists of a polarizing beam splitter (PBS), a PPLN/WR and a half-wave plate (HWP). In the Sagnac interferometer, $|HH\rangle$ and $|VV\rangle$ photon pairs are generated by the clockwise and the anti clockwise directions, respectively. The photon pairs are mixed by PBS and propagate to the opposite direction of the pump laser. The generated quantum state is a polarization entangled BFC corresponding to Eq. (1).

For the evaluation of the quantum states, the two photons are divided at a half beam splitter (BS). Each photon goes to a setup for polarization quantum state tomography with a tunable bandpass filter (BPF). Then they are detected by superconducting nanowire single photon detectors (SNSPDs) [33] (see Methods). We note that in the Sagnac interferometer, unexpected photon pairs $|HV\rangle$ and $|VH\rangle$ are generated by the signal components reflected at the resonator. By placing the PPLN/WR off-center of the interferometer, we postselect only the desired photon pairs composed of the idler photons and the transmitted signal photons by time-resolved coincidence measurement (see Supplementary Information for details).

The frequency correlation of the photon pair over a wide spectrum range is an important property of our quantum frequency comb. To see this, we first measured the joint spectral intensity (JSI) over 80 nm (1520 nm -1600 nm) with the resolution of 3.00 nm, as shown in Fig. 2a. JSIs with higher resolutions of 0.30 nm and 0.03 nm are also shown in Fig. 2b and Fig. 2c. We see that the peaks of the coincidence counts clearly obey the energy conservation and exhibit the frequency correlation

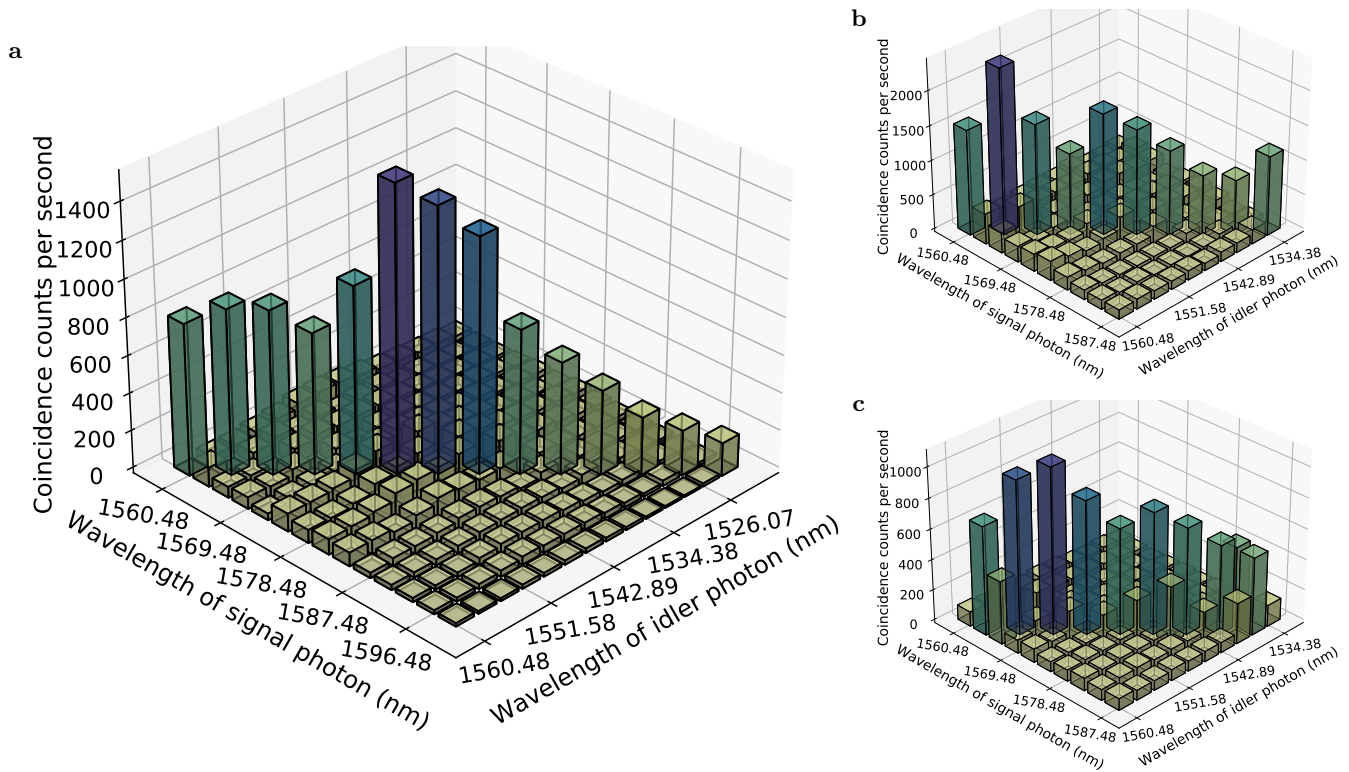


Figure 2: Joint spectral intensity. The coincidence counts among frequency modes with the spectral resolution of **a** 3.00 nm, **b** 0.30 nm, **c** 0.03 nm are shown. The resolutions are selected by BPFs. The peaks appear at the specific frequency combinations satisfying the energy conservation with the pump, signal and idler photons in all frequency range measured, **a** [1560.48 nm, 1599.48 nm] and [1522.43 nm, 1560.48 nm], **b** [1577.13 nm, 1579.83 nm] and [1541.58 nm, 1544.18 nm], **c** [1577.30 nm, 1577.57 nm] and [1543.76 nm, 1544.01 nm]. Note that the range of **b** is equivalent to the spectral resolution of **a** and the range of **c** is the spectral resolution of **b**.

in all frequency range.

Temporal second-order cross-correlation between the signal and the idler photons tells us an additional spectral property of the quantum frequency comb. Figure 3 shows an example of the results for the central wavelengths of 1580.48 nm and 1540.98 nm (see Supplementary Information for other frequency ranges). In the cross-correlation with 3.00 nm filter bandwidth in Fig. 3b, we see a beat signal reflecting the superposition of multiple frequency modes. The beat frequency of 3.5 GHz corresponds to the free spectral range (FSR) of the cavity (see Supplementary Information). On the other hand, when a single frequency mode was picked up by the filters with a 0.03 nm bandwidth corresponding to 3.5 - 3.7 GHz, the beat signal in the delayed coincidence counts disappeared, as shown in Fig. 3a. We estimated the full width at half maximum (FWHM) of the linewidth of the frequency mode around 1580 nm to be $\Delta f_{1/2} = 126$ MHz from the decay time of the cross-correlation. This shows the comb teeth are well separated from each other due to the strong confinement of the signal photons in the resonator. Together with the result in Fig. 2 in which the photon pairs appear over 80 nm (1520 nm - 1600 nm),

the clear beat signal implies the existence of frequency entanglement in the BFC with the frequency mode number of $M \sim 1400$.

The mode number contained in the dense and well separated quantum frequency comb can also be estimated by the temporal second-order autocorrelation function $g^{(2)}(\tau)$ of the signal (idler) photons. The method is well established in the pulsed pump SPDC, but not in the cw pump case. Defining the time-integrated autocorrelation by $\Delta g^{(2)} = \int d\tau (g^{(2)}(\tau) - 1)$, we derived a relation $\Delta g^{(2)} = (\pi \Delta f_{1/2} M)^{-1}$ for the cw-pumped SPDC with the singly resonant cavity, similar to the relation connecting $g^{(2)}$ with the effective mode (Schmidt mode) for the pulsed pump regime [34] (see Methods and Supplementary Information). From the observed $g^{(2)}(\tau)$ with the bandwidths of 0.03 nm and 0.30 nm as shown in Figs. 4a and 4b, we obtained $\Delta g^{(2)} = 2.1$ ns and 0.17 ns, respectively. By using $\Delta f_{1/2} = 126$ MHz, we have estimated M to be 1.2 and 14.9 for bandwidths of 0.03 nm and 0.30 nm, respectively, which is consistent with the mode numbers of 1 and 10 expected from the beat frequency.

Finally, we performed the quantum state tomogra-

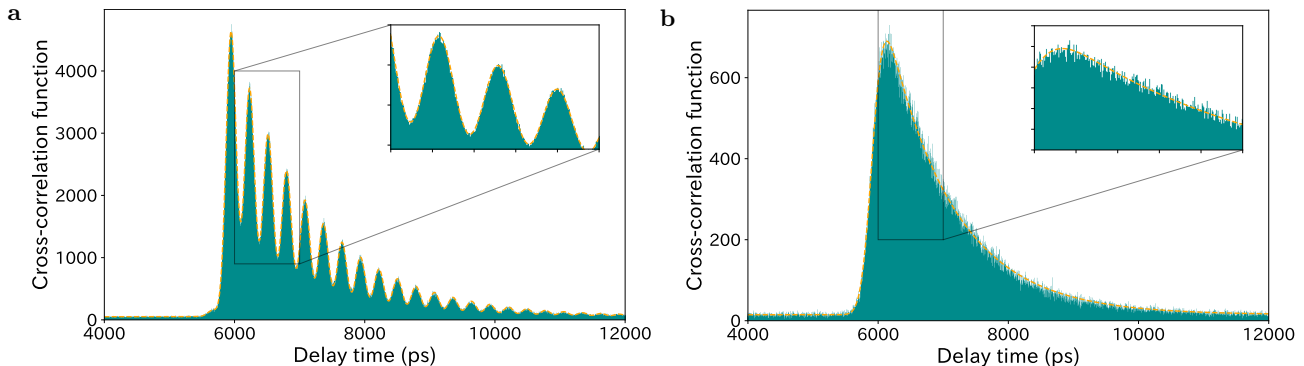


Figure 3: Temporal second-order cross-correlation. The delayed coincidence counts within 4-ps time bin between signal photon and idler photon, which corresponds to the temporal second-order cross-correlation function. The polarizations are fixed to horizontal and the wavelength of signal and idler photon is 1580.48 nm and 1540.98 nm, respectively. The bandwidth of BPFs are **a** 3.00 nm (~ 100 frequency mode) and **b** 0.03 nm (single frequency mode). In **a**, we see the beating of coincidence counts that is a significant evidence of the quantum frequency comb.

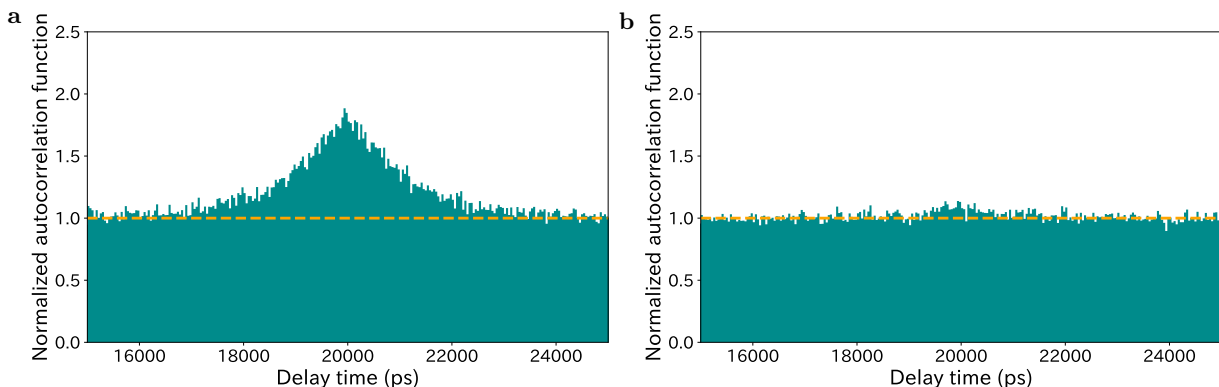


Figure 4: Temporal second-order autocorrelation. The delayed coincidence counts within 40-ps time bin between idler photons, which corresponds to the temporal second-order autocorrelation function. The polarizations are fixed to horizontal. The central wavelength and the bandwidth of the BPFs is set to **a** 1543.76 nm and 0.03 nm and **b** 1543.89 nm and 0.30 nm. The orange lines indicate the normalization factors estimated from the coincidence counts with a large delay. In **a**, since unheralded photons behave like thermal light in the single frequency mode, the bunching effect appears at the zero delay. However, in **b**, it is suppressed by the interference in the multiple frequency modes.

phy of polarization DOF [35] for the various central frequencies. We adjust the pump power to 50 μW , 500 μW and 5 mW for the filter bandwidths of 3.00 nm, 0.30 nm and 0.03 nm, respectively. Examples of the matrix representation of the reconstructed density operators ρ are shown in Fig. 5d-f. We calculated the fidelity defined by $F(\rho) = \max_{\theta} \langle \Psi_{\theta} | \rho | \Psi_{\theta} \rangle$, where $|\Psi_{\theta}\rangle = (|H\rangle|H\rangle + e^{i\theta}|V\rangle|V\rangle)/\sqrt{2}$ is a maximally entangled state with a relative phase θ . As shown in Fig. 5a-c, the observed fidelities for all frequency regions and all bandwidth settings are over 0.7 which clearly exceeds 0.5. This shows the quantum entanglement in polarization subspace exists in all frequency range.

DISCUSSION

We discuss how to improve the fidelity of the observed states. One of the reasons is the contamination of undesired components $|HV\rangle$ and $|VH\rangle$ as is seen in Fig. 7 in Supplementary Information. We can remove the influence by making the difference of the path lengths between the photons being transmitted and the reflected at the PPLN/WR large. Another solution is making the two path lengths the same and stabilizing the interferometer, which leads to not only the fidelity improvement but also doubling the generation rate (see Supplementary Information). The expected fidelities after the improvement are shown in Fig. 5a-c. The remaining decrease of the fidelity will be mainly attributed to the effect of multi-pair generation due to the large pump power. From these results, The pump power of 5 mW would barely sat-

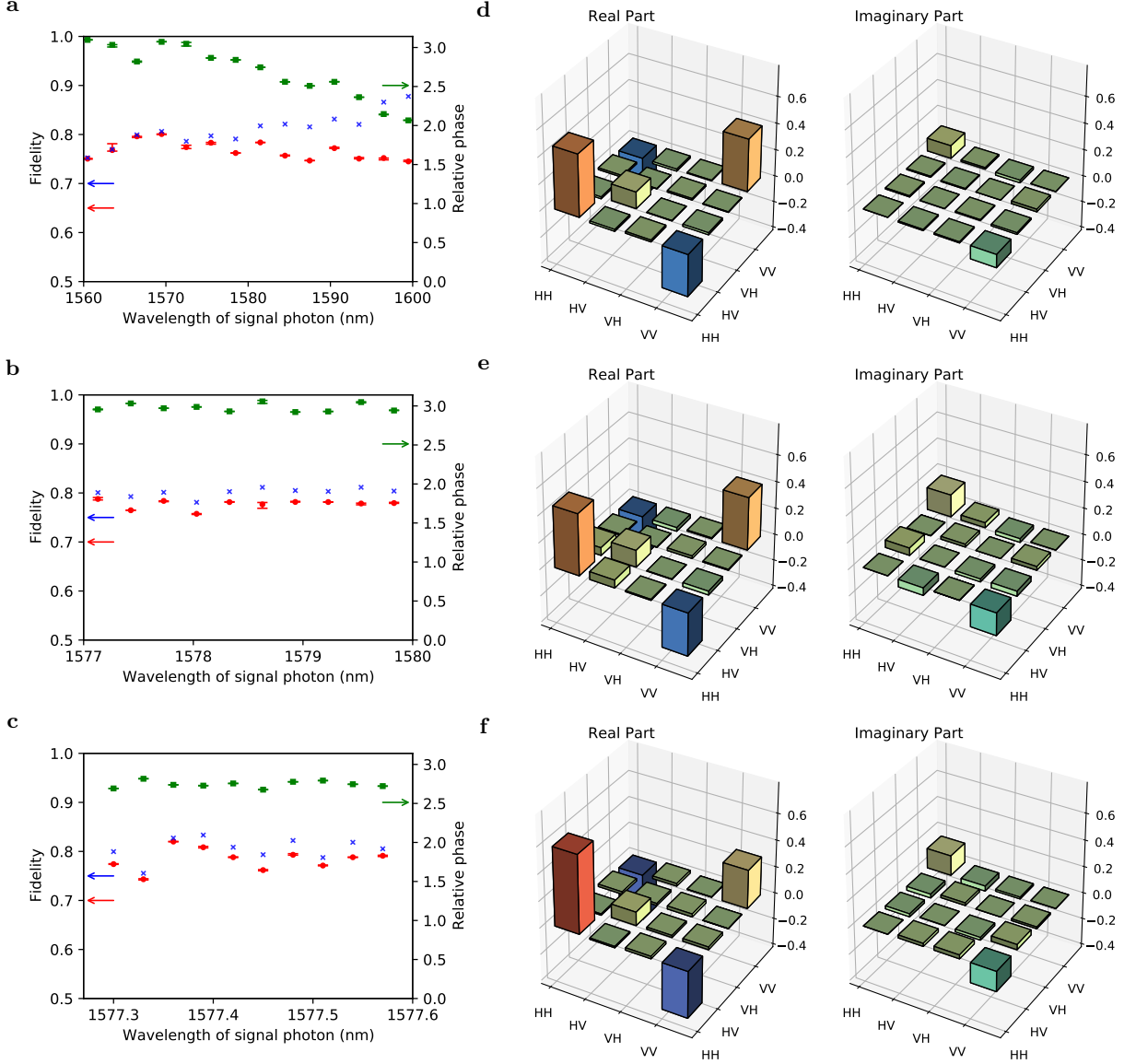


Figure 5: Fidelities and reconstructed density matrices of polarization entangled states. We performed a set of polarization measurements with various central wavelengths and bandwidths of the BPFs. **a-c**, The red markers indicate the fidelities of the quantum state. The green markers indicate the relative phases between the polarizations of HH and VV of the reconstructed states. The blue markers indicate the estimated fidelity which is obtained by removing the effect of the reflected idler photons (see Supplementary Information). The error bars indicate the standard deviations under the assumption of the Poisson statistics of the photon counts. The frequency ranges are **a** [1560.48 nm, 1599.48 nm] and [1522.43 nm, 1560.48 nm], **b** [1571.13 nm, 1579.83 nm] and [1541.58 nm, 1544.18 nm] and **c** [1577.30 nm, 1577.57 nm] and [1543.76 nm, 1544.01 nm] with the bandwidths of 3.00 nm, 0.30 nm and 0.03 nm, which correspond to ~ 100 , 10 and 1 frequency modes, respectively. The example of the reconstructed density matrix is shown in **d**, **e**, **f** with the spectral resolution of 3.00 nm, 0.30 nm, 0.03 nm, respectively. The combination of the frequency modes is **d** 1578.48 nm and 1542.89 nm, **e** 1577.43 nm and 1543.89 nm **f** 1577.39 nm and 1543.93 nm.

isfy $2|\zeta|^2 \ll 1$ and corresponds to the state of Eq. (3). The pump power which achieves the state of Eq. (2) for $M \sim 1400$ will be several μW because ζ is proportional to the pump power.

In conclusion, we achieved the polarization entangled BFC over 1000 frequency modes by using a singly resonant PPLN/WR in a Sagnac interferometer. In addition,

we showed the SPDC-based entangled BFC generator enables us to prepare both the high dimensional hyperentangled photon pair and the frequency-multiplexed entangled photon pairs by adjusting the pump power for SPDC. In both senses, such a massive-mode entangled BFC dramatically enhances the advantage of quantum information processing. Since the millimeter-long cav-

ity structure realizes the comb spacing from GHz to tens of GHz, commercially-available filters and wavelength-division multiplexing devices would be helpful for realizing the further tasks. The versatile, stable and highly efficient system for the generation of the massive-mode entangled BFC will provide a platform for the high-speed and high-efficient quantum information processing.

METHODS

Singly resonant PPLN/WR. we used a 20 mm long ridge waveguide consisting of a Zinc-doped lithium niobate as a core and lithium tantalite as a clad (NTT Electronics) as a nonlinear optical waveguide. The periodically-poling period is designed for satisfying the type-0 quasi-phase-matching of the second harmonic generation of 1560.48 nm light at 35 °C. Both end-faces of the waveguide are flat polished for Fabry-Perot cavity structure, and coated by the dielectric multilayers for a high reflective coating around 1600 nm and anti-reflective coatings around 1520 nm and 780 nm [11]. The waveguide resonator is stabilized by the temperature controll by a Peltier device.

Experimental Setup. The pump light is generated by second harmonic generation in PPLN/W pumped by an external cavity laser with planar lightwave circuit (RIO Planex) at 1560.48 nm. The power and polarization of the pump light are adjusted by a pair of HWPs sandwiching a PBS. In order to keep the effective $M\zeta$ for different bandwidth of BPFs, 3.00 nm, 0.30 nm and 0.03 nm, we set the power of the pump light to 50 μ W, 500 μ W and 5 mW, respectively.

A BFC generated at the Sagnac interferometer is separated from the pump light by a dichroic mirror (DM), and divided into two paths by a beamsplitter (BS) with a probability 1/2. Each photon is projected onto any polarization state using a half-wave plate (HWP), a quarter-wave plate(QWP) and a PBS. The photon is coupled to a single mode fiber connected to a tunable BPF (Alnair Labs), whose bandwidth is adjustable from 0.03 nm to 3.00 nm. Finally, the photon is detected by superconducting nanowire single photon detector (SNSPD) [33]. The electrical signals from the two SNSPDs are used as a start and a stop of a time-to-digital converter (PicoQuant), for recording the coincidence counts with timestamps. For the quantum state tomography, the coincidence counts are totaled up in the time windows of 5800 - 6900 ps.

A formula for estimation of the number of cavity mode in cw pump regime. In pulsed pump regime, it has been founded that the autocorrelation function of signal or idler photons of photon pairs is related the number of effective (Schmidt) modes by $g^{(2)} = 1 + \frac{1}{N}$ under the assumption of an uniform spectral amplitude [34]. However, this formula cannot be directly

applied to cw pumped regime. Instead, in cw pumped regime, the autocorrelation is related to the cavity mode, which is same to the effective mode only in the case of ideal frequency-bin entangled states. A formula we obtained is

$$\begin{aligned} \Delta g^{(2)} &\equiv \int d\tau \left(g^{(2)}(\tau) - 1 \right) \\ &= \frac{1}{M} \frac{\gamma_i^2 + 3\gamma_i\gamma_s + \gamma_s^2}{\gamma_i\gamma_s(\gamma_i + \gamma_s)} \\ &\left(= \begin{cases} \frac{5}{2\gamma_s M} & (\gamma_s = \gamma_i) \\ \frac{1}{\gamma_s M} & (\gamma_s \ll \gamma_i) \end{cases} \right), \end{aligned} \quad (4)$$

where $\gamma_{s(i)} = \pi\Delta f_{1/2}^{s(i)}$ and $\Delta f_{1/2}^{s(i)}$ is FWHM about signal (idler) photon. See Supplementary Information for the derivation.

ACKNOWLEDGEMENTS

R.I., N.I. and T.Yamamoto acknowledge members of Quantum Internet Task Force (QITF) for comprehensive and interdisciplinary discussions of the Quantum Internet. This work was supported by CREST, JST JPMJCR1671; MEXT/JSPS KAKENHI Grant Number JP20H01839, JP18K13483 and JP20J20261; Asahi Glass Foundation; Program for Leading Graduate Schools: Interactive Materials Science Cadet Program.

SUPPLEMENTARY INFORMATION

**Analysis of the state generated from the singly resonant PPLN/WR
and its second-order cross-correlation function**

Here, we briefly summarize theoretical analysis about the photon pair generation by SPDC inside a cavity, which is called cavity-enhanced SPDC [36–43]. Then we explain the fitting function we use for the analysis of the cross-correlation function of the photon pairs and its relation with the spectral properties of the generated BFC. A photon pair generated by cavity-enhanced SPDC is represented by

$$|\Psi\rangle = \int d\omega_i d\omega_s f(\omega_i, \omega_s) a^\dagger(\omega_i) a^\dagger(\omega_s) |0\rangle$$

$$f(\omega_i, \omega_s) \propto \alpha_p(\omega_i + \omega_s) h(L\Delta k) \mathcal{A}(\omega_i) \mathcal{A}(\omega_s). \quad (5)$$

$f(\omega_i, \omega_s)$ is the joint spectral amplitude (JSA) of the signal and idler photon, which is normalized by $\int d\omega_i d\omega_s |f(\omega_i, \omega_s)|^2 = 1$. $\alpha_p(\omega_i + \omega_s)$ is the spectral amplitude of pump light and $h(L\Delta k)$ is the function about the phase-matching condition, where $\Delta k(\omega_i, \omega_s) = n(\omega_i + \omega_s)(\omega_i + \omega_s) - n(\omega_i)\omega_i - n(\omega_s)\omega_s$, L is the length of the nonlinear crystal and n is a refractive index[44]. $\mathcal{A}(\omega)$ is the function representing the transmission spectrum of the cavity [45–47], that is represented as

$$\mathcal{A}(\omega) \propto \sum_{m=0}^{\infty} \frac{\sqrt{\gamma(\omega)}}{\gamma(\omega) - i(\omega - \omega_m)}. \quad (6)$$

Here, FWHM is $\Delta f_{1/2} = \gamma/\pi$ and FSR is $\Delta\omega = \omega_{m+1} - \omega_m = 2Ln(\omega)/c$, where L is the length of the resonator, we assume that is equal to the length of the nonlinear crystal, and c is the speed of light.

In our analysis, we simplify JSA as below. (i) The linewidth of cw pump laser is sufficiently narrow, that is, $\alpha_p(\omega_i + \omega_s) \propto \delta(\omega_p - \omega_i - \omega_s)$. (ii) There are frequency modes m and m' of signal and idler photons satisfying $\omega_m + \omega_{m'} \simeq \omega_p$. It can be achieved by the shift of the pump frequency. (iii) $n(\omega)$ is a constant for the generated photons, leading to the frequency independency of FSR and $h(L\Delta k)$. From (ii) and (iii), only one mode of m' satisfying $\omega_m + \omega_{m'} \simeq \omega_p$ always exists for each m . This means the absence of the cluster effect [48]. In our experiment, the above assumptions are valid because the doubly resonant configuration is only realized in the small frequency range around the degenerated point, 1560.48 nm. Finally, (iv) we neglect frequency dependence of FWHM within the frequency range of measurements, and represent $\gamma(\omega_{s(i)})$ by $\gamma_{s(i)}$. From these assumptions, we obtain

$$f(\omega_i, \omega_s) \propto \delta(\omega_p - \omega_i - \omega_s) \sum_{m, m'} \frac{1}{\gamma_i - i(\omega_i - \omega_m)} \frac{1}{\gamma_s - i(\omega_s - \omega_{m'})}$$

$$= \delta(\omega_p - \omega_i - \omega_s) \sum_m \frac{1}{\gamma_i - i(\omega_i - \omega_m)} \frac{1}{\gamma_s + i(\omega_i - \omega_m)}. \quad (7)$$

In the last equality, we leave only the term about m' satisfying $\omega_{m'} = \omega_p - \omega_m$. The case of $\gamma_i = \gamma_s$ corresponds to the (equally) doubly resonant configuration, and the case of $\gamma_i \rightarrow \infty$ corresponds to the singly resonant configuration where only signal photons are confined.

We next move on to the discussion about cross-correlation measurement for the above state. In the measurement of the coincidence counts between signal and idler photons with a finite temporal resolution, the observed cross-correlation $C_{s,i}$ is described by

$$C_{s,i}^{(1,1)}(\tau) \propto \int d\tau' g_{\sqrt{2}\sigma}(\tau - \tau') G_{s,i}^{(1,1)}(\tau'), \quad (8)$$

where

$$G_{s,i}^{(1,1)}(\tau) \equiv \langle \Psi | a_s(t)^\dagger a_i(t + \tau)^\dagger a_i(t + \tau) a_s(t) | \Psi \rangle \quad (9)$$

is a temporal second-order cross-correlation function, and

$$g_\sigma(t) = \frac{1}{\sqrt{2\pi}\sigma} \exp\left\{-\frac{t^2}{2\sigma^2}\right\} \quad (10)$$

is a function representing a finite temporal resolution of the two photon detectors used for the coincidence measurement, which we assumed a Gaussian function [38].

From Eqs. (5), (7) and (8),

$$C_{s,i}^{(1,1)}(\tau) \propto \int d\tau' g_{\sqrt{2}\sigma}(\tau - \tau') \left| \sum_m \int d\omega_s \frac{e^{-i(\omega_p - \omega_s)\tau'}}{\{\gamma_i + i(\omega_s - \omega_m)\}\{\gamma_s - i(\omega_s - \omega_m)\}} \right|^2 \\ \propto \int d\tau' g_{\sqrt{2}\sigma}(\tau - \tau') \left[e^{-2\gamma_i\tau'} \left| \sum_m e^{i\omega_m\tau'} \right|^2 h(\tau') + e^{2\gamma_s\tau'} \left| \sum_m e^{i\omega_m\tau'} \right|^2 h(-\tau') \right]. \quad (11)$$

$h(\tau)$ is the step function [42]. When we extract a single frequency mode by the BPFs, Eq. (11) becomes

$$C_{s,i,\text{single}}^{(1,1)}(\tau) \propto \int d\tau' g_{\sqrt{2}\sigma}(\tau - \tau') \left(e^{-2\gamma_i\tau'} h(\tau') + e^{2\gamma_s\tau'} h(-\tau') \right) \\ \propto \frac{1}{2} e^{(2\gamma_i\sigma)^2 - 2\gamma_i\tau} \left\{ 1 - \operatorname{erf} \left(-\frac{\tau}{2\sigma} + 2\gamma_i\sigma \right) \right\} + \frac{1}{2} e^{(2\gamma_s\sigma)^2 + 2\gamma_s\tau} \left\{ 1 + \operatorname{erf} \left(-\frac{\tau}{2\sigma} - 2\gamma_s\sigma \right) \right\}, \quad (12)$$

where $\operatorname{erf}(x)$ is a error function. When we extract many frequency modes enough to the approximation

$$\left| \sum_m e^{i\omega_m\tau'} \right| = \left| \sum_m e^{2\pi i m \frac{\tau'}{T_0}} \right| \propto \sum_n \delta(\tau' - nT_0), \quad (13)$$

where $T_0 = 2\pi/\text{FSR}$ represents the round trip time of the cavity, Eq. (11) becomes

$$C_{s,i,\text{multi}}^{(1,1)}(\tau) \propto \frac{1}{2\sqrt{\pi}\sigma} \left[\exp\left(\frac{-\tau^2}{4\sigma^2}\right) + \sum_{j=1}^{\infty} \left[\exp\left(-2\gamma_i j T_0 - \frac{(jT_0 - \tau)^2}{4\sigma^2}\right) + \exp\left(-2\gamma_s j T_0 - \frac{(jT_0 + \tau)^2}{4\sigma^2}\right) \right] \right]. \quad (14)$$

We note that if the biphoton state is the maximally mixed state of the frequency modes, the coincidence counts is represented by Eq. (12). From this, it may be possible to consider the influence of the decoherence on the frequency modes by using the combination of Eqs.(12) and (14) with the normalization factor,

$$C_{s,i,\text{sum}}^{(1,1)}(\tau) \propto p \frac{(1 - e^{-2\gamma_i T})(1 - e^{-2\gamma_s T})}{1 - e^{-2(\gamma_i + \gamma_s)T}} C_{s,i,\text{multi}}^{(1,1)}(\tau) + (1 - p) \frac{2\gamma_i\gamma_s}{\gamma_i + \gamma_s} C_{s,i,\text{single}}^{(1,1)}(\tau). \quad (15)$$

In our experiment, $p \simeq 1$ was estimated, and this means that the influence of the decoherence is negligibly small.

Analysis of the state generated from the Sagnac interferometer and its fidelity

Here we discuss the polarization entangled state in our experiment in details. We consider only one photon pair state generated by SPDC. As shown in Fig. 6, due to the cavity structure for the signal photons, H-polarized and V-polarized pump light respectively generate photon pairs described by

$$g_H e^{i(\omega_p\tau_l + \theta(\omega_p))} (t_l |V\rangle_{ir} |V\rangle_{sr} + r_l |V\rangle_{ir} |V\rangle_{sl}), \quad (16)$$

$$g_V e^{i\omega_p\tau_r} (t_r |V\rangle_{il} |V\rangle_{sl} + r_r |V\rangle_{il} |V\rangle_{sr}), \quad (17)$$

where $g_{H(V)}$ is the coupling constant proportional to the complex amplitude of the H (V)-polarized pump light, $\theta(\omega)$ is the frequency-dependent phases from a multi-order HWP, and $\tau_{l(r)}$ is the propagation time of the left (right) arm of Sagnac interferometer in Fig. 6. $t_{l(r)}$ and $r_{l(r)}$ are transmittance and reflectance of PPLN/WR when the light enters it from the left (right) side, respectively, where $|t_{l(r)}|^2 + |r_{l(r)}|^2 = 1$ holds. The output state just before the photon detection is represented by

$$|\Psi\rangle \propto g_H \eta_{ir} e^{i(\omega_p\tau_l + \theta(\omega_p) + \omega_i\tau_r)} \left(t_l \eta_{sr} e^{i(\omega_s\tau_r)} |V\rangle_i |V\rangle_s + r_l \eta_{sl} e^{i(\omega_s\tau_l + \theta(\omega_s))} |V\rangle_i |H\rangle_s \right) \\ + g_V \eta_{il} e^{i(\omega_p\tau_r + \omega_i\tau_l + \theta(\omega_i))} \left(t_r \eta_{sl} e^{i(\omega_s\tau_l + \theta(\omega_s))} |H\rangle_i |H\rangle_s + r_r \eta_{sr} e^{i\omega_s\tau_r} |H\rangle_i |V\rangle_s \right) \\ \propto g_H \eta_{ir} |V\rangle_i (t_l \eta_{sr} |V\rangle_s + r_l \eta_{sl} e^{-i\Delta\theta} |H\rangle_s) + g_V \eta_{il} e^{i\phi} |H\rangle_i (t_r \eta_{sl} |H\rangle_s + r_r \eta_{sr} e^{i\Delta\theta} |V\rangle_s), \quad (18)$$

$$\phi = \theta(\omega_s) + \theta(\omega_i) - \theta(\omega_p), \quad \Delta\tau = \tau_r - \tau_l, \quad \Delta\theta = \omega_s\Delta\tau - \theta(\omega_s), \quad (19)$$

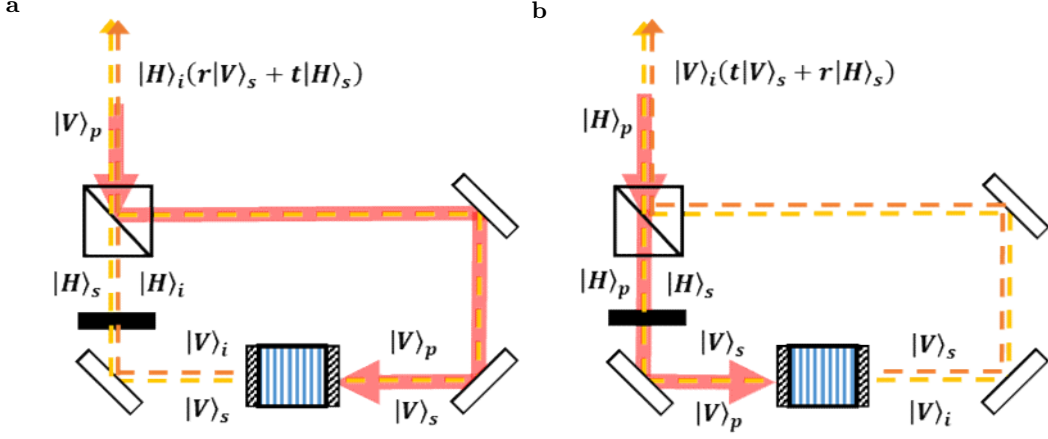


Figure 6: Sagnac interferometer with cavity-enhanced spontaneous parametric down-conversion. **a** The V-polarized pump laser, the H-polarized idler photon and the transmitted H-polarized signal photon propagate clockwise; the reflected V-polarized signal photon propagates counterclockwise. **b** The H-polarized pump laser, the V-polarized idler photon and the transmitted V-polarized signal photon propagate counterclockwise; the reflected H-polarized signal photon propagates clockwise.

where $\eta_{i(j)l(r)}$ is total loss in the optical circuit for the signal (idler) photons coming from the left (right) side of the PPLN/WR. By setting the polarization of the pump light so as to satisfy $g_H \eta_{ir} t_l \eta_{sr} = g_V \eta_{il} t_r \eta_{sl}$, we obtain

$$|\Psi\rangle \propto |V\rangle_i (|V\rangle_s + \beta_H e^{-i\Delta\theta} |H\rangle_s) + e^{i\phi} |H\rangle_i (|H\rangle_s + \beta_V e^{i\Delta\theta} |V\rangle_s), \quad (20)$$

where

$$\beta_H \equiv \frac{r_l \eta_{sl}}{t_l \eta_{sr}}, \quad \beta_V \equiv \frac{r_r \eta_{sr}}{t_r \eta_{sl}}. \quad (21)$$

In case of $\Delta\tau \gg 0$, we obtain the maximally polarization entangled state $|\Phi\rangle \equiv 1/\sqrt{2}(|H\rangle_i |H\rangle_s + e^{i\phi} |V\rangle_i |V\rangle_s)$ ideally. But in our experiment, there is the overlap between $|V\rangle_i |H\rangle_s$ and $|\Phi\rangle$ as shown in Fig. 7. For the estimation of these effect on the fidelity, we consider the delay time dependency of the generated state as

$$|\Psi(\tau)\rangle \propto |V, t\rangle_i \left(e^{-\gamma\tau} h(\tau) |V, t + \tau\rangle_s + \beta_H e^{-i\Delta\theta} e^{-\gamma(\tau + \Delta\tau)} h(\tau + \Delta\tau) |H, t + \tau\rangle_s \right) + e^{i\phi} |H, t\rangle_i \left(e^{-\gamma\tau} h(\tau) |H, t + \tau\rangle_s + \beta_V e^{i\Delta\theta} e^{-\gamma(\tau - \Delta\tau)} h(\tau - \Delta\tau) |V, t + \tau\rangle_s \right). \quad (22)$$

Here, we approximated the temporal shaping of the state by $e^{-\gamma\tau}$. In our experiment, we pick up the time windows from 0 to $\Delta\tau$, that is

$$|\bar{\Psi}\rangle \equiv \int_0^{\Delta\tau} d\tau |\Psi(\tau)\rangle \propto |\Phi\rangle + \frac{\beta_H}{\sqrt{2}} e^{-\gamma\Delta\tau - i\Delta\theta} |V\rangle_i |H\rangle_s. \quad (23)$$

Here, we redefined as

$$|H(V)\rangle_i |H(V)\rangle_s \equiv \int_0^{\Delta\tau} e^{-\gamma\tau} |H(V), t\rangle_i |H(V), t + \tau\rangle_s. \quad (24)$$

In addition, the randomization of the phase of the component $|V\rangle_i |H\rangle_s$ leads

$$\rho_{\bar{\Psi}} \propto \left(|\Phi\rangle \langle\Phi| + \frac{|\beta_H|^2}{2} e^{-2\gamma\Delta\tau} |VH\rangle \langle VH|_{is} \right). \quad (25)$$

From the definition of fidelity $F(\rho) \equiv \max_{\theta} \langle\Psi_{\theta}|\rho|\Psi_{\theta}\rangle$, where $|\Psi_{\theta}\rangle \equiv 1/\sqrt{2}(|HH\rangle + e^{i\theta} |VV\rangle)$,

$$F(\rho_{\bar{\Psi}}) = \left(1 + \frac{|\beta_H|^2}{2} e^{-2\gamma\Delta\tau} \right)^{-1} \quad (26)$$

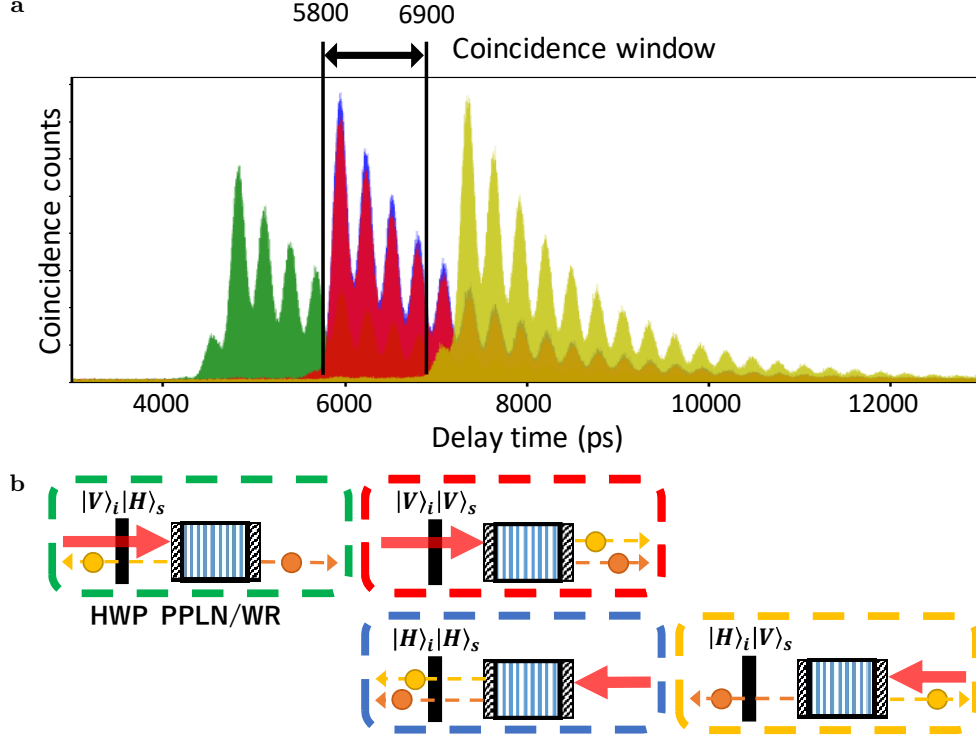


Figure 7: Correspondence of the arrival time, path and polarization of four output states. **a** The experimental data of coincidence counts in four different polarization settings, HH (blue), VV (red), VH (green) and HV (yellow). VH (HV) photon pairs are detected earlier (later) than the VV and HH photon pairs. **b** The paths of the polarizing photons in the Sagnac interferometer (see also Fig. 6). The difference of the arrival times are originated from the difference of the propagation paths.

holds. From these results, we estimated the fidelity expected in the case of $\Delta\tau \gg 0$ by multiplying $F(\rho_{\overline{\Psi}})^{-1}$ to the experimentally measured fidelity (see Fig. 5 in the manuscript). From the best fit to the data of the temporal cross-correlation in the every polarization and frequency ranges, we extracted γ and β_H , which is estimated as the ratio of the amplitude between VH and HH components.

Analysis of the generated polarization entangled BFC

In the manuscript, we discussed about the simplified model for generating polarization entangled BFC. Here let us analyze the polarization entangled BFC generated in the experiment with a more realistic model. As well as Eq. (5), the time evolution of the cavity-enhanced SPDC for arbitrary pump power is represented by

$$|\Psi\rangle \propto \exp\left[g_{H(V)} \int d\omega_i d\omega_s f_{H(V)}(\omega_i, \omega_s) a_{H(V)}^\dagger(\omega_i) a_{H(V)}^\dagger(\omega_s) - h.c.\right] |0\rangle \equiv U_{H(V)} |0\rangle. \quad (27)$$

Eq. (27) is approximately reduced to Eq. (5) when $|g|^2 \ll 1$ is satisfied. In cw pump regime, JSA $f_{H(V)}(\omega_i, \omega_s)$ cannot be decomposed like $\sum_m c_{H(V),m} f_{H(V),m}(\omega_i) f'_{H(V),m}(\omega_s)$. Instead, from assumption (i) above, we decompose JSA as

$$f_{H(V)}(\omega_i, \omega_s) \propto \delta(\omega_p - \omega_i - \omega_s) \sum_m c_{H(V),m} f_{H(V),m}(\omega_i). \quad (28)$$

$c_{H(V),m}$ is a coefficient of each cavity mode and $f_{H(V),m}(\omega_i)$ is normalized by $\int d\omega_i |f_{H(V),m}(\omega_i)|^2 = 1$. Assuming that each frequency mode is well separated from each other, that is, $\int d\omega_i f_{H(V),m}^*(\omega_i) f_{H(V),m'}(\omega_i) \simeq \delta_{m,m'}$. The generation processes of each cavity mode is independent as

$$U_{H(V)} |0\rangle \simeq \prod_m \exp\left[g_{H(V)} c_{H(V),m} \int d\omega_i f_{H(V),m}(\omega_i) a_{H(V)}^\dagger(\omega_i) a_{H(V)}^\dagger(\omega_p - \omega_i) - h.c.\right] |0\rangle \equiv \prod_m U_{H(V),m} |0\rangle. \quad (29)$$

Modifying Eq. (20) to the case of arbitrary pump power using the above results, the state generated by our experiments can be represented as

$$|\Psi\rangle = \prod_m U_{H,m} U_{V,m} |0\rangle, \quad (30)$$

where we ignored the component of the reflected signal photons. In the case of $|g_{HC_{H,m}}|^2 + |g_{VC_{V,m}}|^2 \ll 1$, the state of Eq. (30) is approximately

$$|\Psi\rangle \simeq \bigotimes_m \frac{1}{\sqrt{1 + |g_{HC_{H,m}}|^2 + |g_{VC_{V,m}}|^2}} \left(1 + g_{HC_{H,m}} \int d\omega_i f_{H,m}(\omega_i) a_H^\dagger(\omega_i) a_H^\dagger(\omega_p - \omega_i) + g_{VC_{V,m}} \int d\omega_i f_{V,m}(\omega_i) a_V^\dagger(\omega_i) a_V^\dagger(\omega_p - \omega_i) \right) |0\rangle_m. \quad (31)$$

This state can be regarded as a frequency-multiplexed entangled photon pair as well as the state in Eq. (3) of the manuscript. On the other hand, when $\sum_m (|g_{HC_{H,m}}|^2 + |g_{VC_{V,m}}|^2) \ll 1$ is satisfied, the state is approximately,

$$|\Psi\rangle \simeq \frac{1}{\sqrt{1 + \sum_m (|g_{HC_{H,m}}|^2 + |g_{VC_{V,m}}|^2)}} \left(1 + \sum_m \left(g_{HC_{H,m}} \int d\omega_i f_{H,m}(\omega_i) a_H^\dagger(\omega_i) a_H^\dagger(\omega_p - \omega_i) + g_{VC_{V,m}} \int d\omega_i f_{V,m}(\omega_i) a_V^\dagger(\omega_i) a_V^\dagger(\omega_p - \omega_i) \right) \right) |0\rangle. \quad (32)$$

After removing the vacuum state, this state may correspond to the state in Eq. (2) of the manuscript, but this state is not a exact frequency-bin entangled state because the spectral correlation between signal and idler photons remains in each bin. When the FWHM of the generated BFC is much smaller than the FWHM of pump laser, the spectral correlation between signal and idler photons in each bin can be neglected and the exact frequency-bin entangled state, which is written like $M^{-1/2} \sum_{m=1}^M |\omega_{i,m}\rangle |\omega_{s,m}\rangle$, can be generated. Therefore, pulsed pump regime superiors to cw pump regime about the hyperentanglement state generation.

Theory of the autocorrelation function and the cavity mode in cw pump regime

It is discovered in ref.[34] that a value $g^{(2)}$ relevant to $g^{(2)}(\tau)$ of the signal or idler photon of a photon pair in the pulse pump regime, is related to the number of effective mode of the photon pair. Here the effective mode means the Schmidt mode of continuous variable Schmidt decomposition [49, 50]. Under the assumption of an uniform spectral amplitude, the relation between $g^{(2)}$ and the number of the effective mode N is written by $g^{(2)} = 1 + \frac{1}{N}$. A similar discussion is held in the cw pump regime [42] in which $g^{(2)}(0) \simeq 1 + \frac{1}{M}$ was derived with the assumption of the detectors having the finite temporal resolution, where M represents the number of the cavity mode. These results look giving the same formula and have been applied for many experiments using pulse laser [7, 51] and cw laser [28, 52, 53]. Here we show another formula for the cw pump regime, which is independent of the temporal resolution of the detectors.

From Eq. (7), we define $f(\omega_i)$ and $f_m(\omega_i)$ as

$$f(\omega_i, \omega_s) \equiv \delta(\omega_p - \omega_i - \omega_s) f(\omega_i) \equiv \delta(\omega_p - \omega_i - \omega_s) \frac{1}{\sqrt{M}} \sum_{m=1}^M f_m(\omega_i), \quad (33)$$

$f(\omega_i)$ and $f_m(\omega_i)$ are normalized. $f_m(\omega_i)$ represents normalized spectral amplitude of each cavity mode and we assumed that the each cavity mode is orthogonal. We calculate second-order autocorrelation function of the idler photons of the photon pairs as

$$G_{i,i}^{(2)}(\tau) = \langle \Psi | a_i(t)^\dagger a_i(t + \tau)^\dagger a_i(t + \tau) a_i(t) | \Psi \rangle. \quad (34)$$

By using the second order term of Eq. (27) without the polarization dependency as the lowest-order approximation

for $|\Psi\rangle$, we obtain

$$\begin{aligned}
& G_{i,i}^{(2)}(\tau) \\
& \propto \left\| a_i(t+\tau)a_i(t) \int d\omega_{i1} \int d\omega_{i2} f(\omega_{i1})f(\omega_{i2})a_i^\dagger(\omega_{i1})a_s^\dagger(\omega_p-\omega_{i1})a_i^\dagger(\omega_{i2})a_s^\dagger(\omega_p-\omega_{i2})|0\rangle \right\|^2 \\
& = \left\| \frac{1}{2\pi} \int d\omega_{i1} \int d\omega_{i2} f(\omega_{i1})f(\omega_{i2})(e^{i\omega_{i1}\tau} + e^{i\omega_{i2}\tau})a_s^\dagger(\omega_p-\omega_{i1})a_s^\dagger(\omega_p-\omega_{i2})|0\rangle \right\|^2 \\
& = \frac{2}{(2\pi)^2} \int d\omega_{i1} \int d\omega_{i2} |f(\omega_{i1})|^2 |f(\omega_{i2})|^2 (2 + e^{i(\omega_{i1}-\omega_{i2})\tau} + e^{-i(\omega_{i1}-\omega_{i2})\tau}) \\
& = \frac{1}{\pi^2} \left[\left| \int d\omega_i |f(\omega_i)|^2 \right|^2 + \left| \int d\omega_i |f(\omega_i)|^2 e^{-i\omega_i\tau} \right|^2 \right] \\
& = \frac{1}{\pi^2} \left[1 + 2\pi \left| \mathcal{F}[|f(\omega_i)|^2](\tau) \right|^2 \right]. \tag{35}
\end{aligned}$$

where $\mathcal{F}[|f(\omega_i)|^2]$ is a Fourier transformation of the spectral intensity of the idler photon. When we define the normalized autocorrelation function as $g_{i,i}^{(2)}(\tau) \equiv G_{i,i}^{(2)}(\tau)/G_{i,i}^{(2)}(\tau \rightarrow \infty)$, we obtain

$$g_{i,i}^{(2)}(\tau) = 1 + 2\pi \left| \mathcal{F}[|f(\omega_i)|^2](\tau) \right|^2. \tag{36}$$

This result shows $g_{i,i}^{(2)}(0) = 2$, which is independent from the spectral characteristics of the photon pairs. In the single mode case [42], Eq. (36) is calculated as

$$g_{i,i}^{(2)}(\tau) = 1 + \left| \frac{1}{\gamma_i - \gamma_s} (\gamma_i e^{-\gamma_s|\tau|} - \gamma_s e^{-\gamma_i|\tau|}) \right|^2. \tag{37}$$

In the multi-mode case, $g_{i,i}^{(2)}(\tau)$ becomes more complex, so we alternatively define

$$\Delta g_{i,i}^{(2)} \equiv \int d\tau (g_{i,i}^{(2)}(\tau) - 1). \tag{38}$$

The range of temporal integral is assumed to be sufficiently large. From Eq. (36),

$$\Delta g_{i,i}^{(2)} = 2\pi \int d\tau \left| \mathcal{F}[|f(\omega_i)|^2](\tau) \right|^2 = 2\pi \int d\omega_i |f(\omega_i)|^4. \tag{39}$$

Substituting Eq. (33) to Eq. (39), we obtain

$$\begin{aligned}
\Delta g_{i,i}^{(2)} &= \frac{2\pi}{M^2} \sum_m \int d\omega_i |f_m(\omega_i)|^4 \\
&= \frac{2\pi}{M} \left\{ \int d\omega \frac{1}{(\gamma_i^2 + \omega^2)^2} \frac{1}{(\gamma_s^2 + \omega^2)^2} \right\} \left\{ \int d\omega \frac{1}{\gamma_i^2 + \omega^2} \frac{1}{\gamma_s^2 + \omega^2} \right\}^{-2} \\
&= \frac{1}{M} \frac{\gamma_i^2 + 3\gamma_i\gamma_s + \gamma_s^2}{\gamma_i\gamma_s(\gamma_i + \gamma_s)} \tag{40}
\end{aligned}$$

$$= \begin{cases} \frac{5}{2\gamma_s M} & (\gamma_s = \gamma_i) \\ \frac{1}{\gamma_s M} & (\gamma_s \ll \gamma_i) \end{cases}. \tag{41}$$

Therefore, if γ_i and γ_s are known, it is possible to estimate the number of cavity modes from this formula. As well as Eq. (8), the actual value obtained from the measurement is written by

$$C_{i,i}^{(2)}(\tau) \propto \int d\tau' g_{\sqrt{2}\sigma}(\tau - \tau') G_{i,i}^{(2)}(\tau'). \tag{42}$$

After the integration about the time, we obtain $\Delta g_{i,i}^{(2)}$ in Eq. (38),

$$\int d\tau (C_{i,i}^{(2)}(\tau) - C_{i,i}^{(2)}(\tau \rightarrow \infty)) \propto \int d\tau (G_{i,i}^{(1,1)}(\tau) - G_{i,i}^{(1,1)}(\tau \rightarrow \infty)) \propto \Delta g_{i,i}^{(2)}. \tag{43}$$

Therefore, $\Delta g_{i,i}^{(2)}$ is measurable without depending on the temporal resolution of the detectors.

Table I: The estimated properties of the generated frequency comb. FSRs and FWHMs of the generated frequency combs in different frequency ranges are estimated from the best fit to the temporal cross-correlation measurements. Finesse and Q factor are calculated from these values. () indicates the data of idler photon in a doubly resonant case.

Wavelength	FSR	FWHM	Finesse	Q factor
1560 nm	3.5 GHz	516(453) MHz	7(8)	$3.7(4.2) \times 10^5$
1570 nm	3.5 GHz	243(1043) MHz	15(3)	$7.9(1.8) \times 10^5$
1580 nm	3.5 GHz	126 MHz	28	1.5×10^6
1590 nm	3.5 GHz	85 MHz	41	2.2×10^6
1600 nm	3.5 GHz	57 MHz	62	3.3×10^6

Full data of time histogram of coincidence counts and estimated property of frequency comb

We performed the measurement of the time histogram of coincidence counts in each frequency range, setting the central wavelength of the BPFs to (1560.48 nm, 1560.48 nm), (1570.48 nm, 1550.61 nm), (1580.48 nm, 1540.98 nm), (1590.48 nm, 1531.59 nm) and (1600.48 nm, 1522.43 nm), and the bandwidths of the BPFs to 3.00 nm and 0.03 nm. Figure S6 shows the all results with the fitting using Eq. (15) for the bandwidth of 3.00 nm and Eq. (12) for the bandwidth of 0.03 nm. The fitting results show $p \simeq 1$ in Eq. (15) and the results of the fitting using Eq. (15) are almost same to the results of the fitting using Eq. (14). Therefore, the generated states are almost pure states. The property of the generated frequency comb, which is estimated by the best fit to the data, are shown in Table. I. The FWHM depends on the frequency because FWHM is related to the frequency dependent reflectance of PPLN/WR [11].

Another method for generating the polarization entangled state using all polarization components

From Eq. (20), we can utilize the whole state as the polarization entangled state by setting the length of arms of Sagnac interferometer to the same: $\tau_r = \tau_l$ with stabilization of the relative phase. The inner product of the two terms in Eq. (20) satisfies

$$\langle V|_s + \beta_H^* e^{i\Delta\theta} \langle H|_s \rangle (|H\rangle_s + \beta_V e^{i\Delta\theta} |V\rangle_s) \propto r_l^* t_r (\eta_{sl}^2 - \eta_{sr}^2), \quad (44)$$

where we used the relation $r_l^* t_r + t_l^* r_r = 0$. Therefore, in the symmetric loss case, that is $\eta_{sl} = \eta_{sr}$, the state in Eq. (20) is the maximally entangled state. Asymmetric losses, however, degrade the orthogonality and cause the decrease of the fidelity to the maximally entangled state. A lower bound of its fidelity is

$$F \geq \frac{1}{2} \left[1 + |1 - \beta_H \beta_V| \sqrt{(1 + |\beta_H|^2)(1 + |\beta_V|^2)} \right] \\ = \frac{1}{2} \left[1 + \left\{ \left(1 + |r|^2 \left(\frac{\eta_{sl}^2}{\eta_{sr}^2} - 1 \right) \right) \left(1 + |r|^2 \left(\frac{\eta_{sr}^2}{\eta_{sl}^2} - 1 \right) \right) \right\}^{-1/2} \right]. \quad (45)$$

In the second equation, $|r_r| = |r_l| \equiv |r|$, $|t_r| = |t_l| \equiv |t|$, $|r|^2 + |t|^2 = 1$ and $1 - \beta_H \beta_V = 1 - r_r r_l / t_r t_l = |t|^{-2}$ are used. This lower bound is almost 1 in usual experiments and this method will work well. This approach has twice generation rate and does not require the temporary distinction.

* ikuta@mp.es.osaka-u.ac.jp

† yamamoto@mp.es.osaka-u.ac.jp

[1] N. Gisin and R. Thew, Quantum communication, *Nature Photonics* **1**, 165 (2007).

[2] J. Yin, Y. Cao, Y. H. Li, S. K. Liao, L. Zhang, J. G. Ren, W. Q. Cai, W. Y. Liu, B. Li, H. Dai, G. B. Li, Q. M. Lu, Y. H. Gong, Y. Xu, S. L. Li, F. Z. Li, Y. Y. Yin,

Z. Q. Jiang, M. Li, J. J. Jia, G. Ren, D. He, Y. L. Zhou, X. X. Zhang, N. Wang, X. Chang, Z. C. Zhu, N. L. Liu, Y. A. Chen, C. Y. Lu, R. Shu, C. Z. Peng, J. Y. Wang, and J. W. Pan, Satellite-based entanglement distribution over 1200 kilometers, *Science* **356**, 1140 (2017).

[3] P. Kok, W. J. Munro, K. Nemoto, T. C. Ralph, J. P. Dowling, and G. J. Milburn, Review article: Linear optical quantum computing, *Reviews of Modern Physics* **79**, 135 (2005).

[4] J. M. Lukens and P. Lougovski, Frequency-encoded pho-

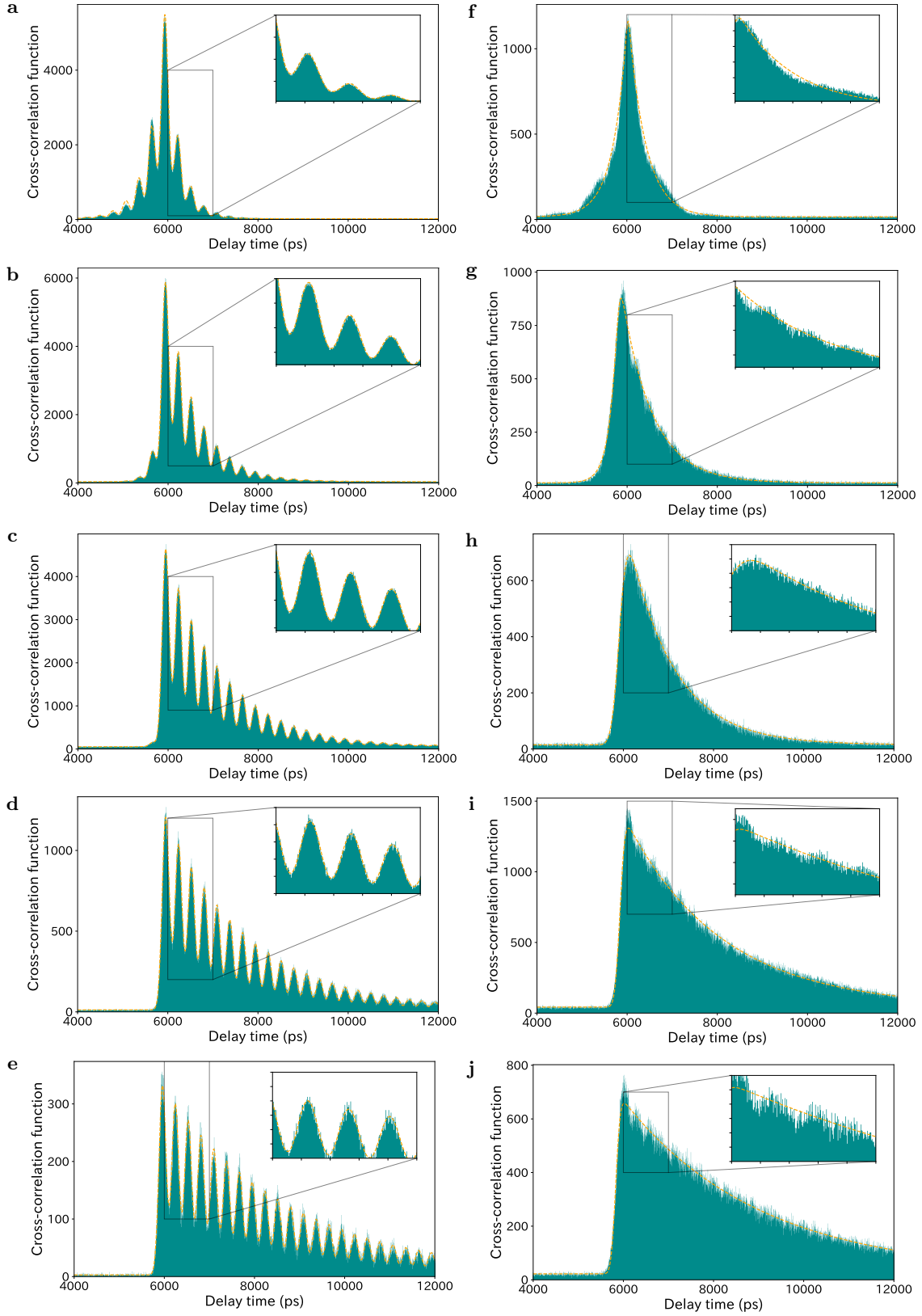


Figure 8: Full data of temporal second-order cross-correlation. The delayed coincidence counts within 4-ps time bin between signal photon and idler photon, which corresponds to the temporal second-order cross-correlation function. The polarizations are fixed to horizontal. The bandwidths of BPFs are **a-e** 0.03 nm (single frequency mode) and **f-j** 3.00 nm (~ 100 frequency mode). The wavelengths are **a,f** (1560.48 nm, 1560.48 nm), **b,g** (1570.48 nm, 1550.61 nm), **c,h** (1580.48 nm, 1540.98 nm), **d,i** (1590.48 nm, 1531.59 nm) and **e,j** (1600.48 nm, 1522.43 nm).

- tonic qubits for scalable quantum information processing, *Optica* **4**, 8 (2017).
- [5] V. Giovannetti, S. Lloyd, and L. MacCone, Advances in quantum metrology, *Nature Photonics* **5**, 222 (2011).
- [6] T. Kobayashi, R. Ikuta, S. Yasui, S. Miki, T. Yamashita, H. Terai, T. Yamamoto, M. Koashi, and N. Imoto, Frequency-domain Hong–Ou–Mandel interference, *Nature Photonics* **10**, 441 (2016).
- [7] M. Kues, C. Reimer, P. Roztocki, L. R. Cortés, S. Sciara, B. Wetzel, Y. Zhang, A. Cino, S. T. Chu, B. E. Little, D. J. Moss, L. Caspani, J. Azaña, and R. Morandotti, On-chip generation of high-dimensional entangled quantum states and their coherent control, *Nature* **546**, 622 (2017).
- [8] L. Caspani, C. Reimer, M. Kues, P. Roztocki, M. Clerici, B. Wetzel, Y. Jestin, M. Ferrera, M. Peccianti, A. Pasquazi, L. Razzari, B. E. Little, S. T. Chu, D. J. Moss, and R. Morandotti, Multifrequency sources of quantum correlated photon Pairs on-chip: A path toward integrated Quantum Frequency Combs, *Nanophotonics* **5**, 351 (2016).
- [9] M. Kues, C. Reimer, J. M. Lukens, W. J. Munro, A. M. Weiner, D. J. Moss, and R. Morandotti, Quantum optical microcombs, *Nature Photonics* **13**, 170 (2019).
- [10] P. Many, J. A. Jaramillo-Villegas, O. D. Odele, K. Han, D. E. Leaird, J. M. Lukens, P. Lougovski, M. Qi, and A. M. Weiner, 50-GHz-spaced comb of high-dimensional frequency-bin entangled photons from an on-chip silicon nitride microresonator, *Optics Express* **26**, 1825 (2018).
- [11] R. Ikuta, R. Tani, M. Ishizaki, S. Miki, M. Yabuno, H. Terai, N. Imoto, and T. Yamamoto, Frequency-Multiplexed Photon Pairs Over 1000 Modes from a Quadratic Nonlinear Optical Waveguide Resonator with a Singly Resonant Configuration, *Physical Review Letters* **123**, 193603 (2019).
- [12] G. Maltese, M. I. Amanti, F. Appas, G. Sinnl, A. Lemaître, P. Milman, F. Baboux, and S. Ducci, Generation and symmetry control of quantum frequency combs, *npj Quantum Information* **6**, 13 (2020).
- [13] H. H. Lu, J. M. Lukens, N. A. Peters, O. D. Odele, D. E. Leaird, A. M. Weiner, and P. Lougovski, Electro-Optic Frequency Beam Splitters and Tritters for High-Fidelity Photonic Quantum Information Processing, *Physical Review Letters* **120**, 30502 (2018).
- [14] H.-H. Lu, J. M. Lukens, B. P. Williams, P. Many, N. A. Peters, A. M. Weiner, and P. Lougovski, A controlled-NOT gate for frequency-bin qubits, *npj Quantum Information* **5**, 24 (2019).
- [15] C. Reimer, S. Sciara, P. Roztocki, M. Islam, L. Romero Cortés, Y. Zhang, B. Fischer, S. Loranger, R. Kashyap, A. Cino, S. T. Chu, B. E. Little, D. J. Moss, L. Caspani, W. J. Munro, J. Azaña, M. Kues, and R. Morandotti, High-dimensional one-way quantum processing implemented on d-level cluster states, *Nature Physics* **15**, 148 (2019).
- [16] R. Ikuta, T. Kobayashi, T. Yamazaki, N. Imoto, and T. Yamamoto, A cavity-enhanced broadband photonic Rabi oscillation (2020), arXiv:2008.01280.
- [17] Z. Xie, T. Zhong, S. Shrestha, X. A. Xu, J. Liang, Y. X. Gong, J. C. Bienfang, A. Restelli, J. H. Shapiro, F. N. Wong, and C. W. Wong, Harnessing high-dimensional hyperentanglement through a biphoton frequency comb, *Nature Photonics* **9**, 536 (2015).
- [18] K. C. Chang, X. Cheng, M. C. Sarihan, A. Kumar, Y. S. Lee, T. Zhong, Y. X. Gong, Z. Xie, J. H. Shapiro, F. N. C. Wong, and C. W. Wong, 648 Hilbert space dimensionality in a biphoton frequency comb, arXiv:2005.07759 (2020).
- [19] C. Reimer, M. Kues, P. Roztocki, B. Wetzel, F. Grazioso, B. E. Little, S. T. Chu, T. Johnston, Y. Bromberg, L. Caspani, D. J. Moss, and R. Morandotti, Generation of multiphoton entangled quantum states by means of integrated frequency combs, *Science* **351**, 1176 (2016).
- [20] F.-G. Deng, B.-C. Ren, and X.-H. Li, Quantum hyperentanglement and its applications in quantum information processing, *Science Bulletin* **62**, 46 (2017).
- [21] P. G. Kwiat and H. Weinfurter, Embedded Bell-state analysis, *Physical Review A* **58**, R2623 (1998).
- [22] J. T. Barreiro, T.-C. Wei, and P. G. Kwiat, Beating the channel capacity limit for linear photonic superdense coding, *Nature Physics* **4**, 282 (2008), arXiv:1009.5128.
- [23] Y.-B. Sheng and F.-G. Deng, Deterministic entanglement purification and complete nonlocal Bell-state analysis with hyperentanglement, *Physical Review A* **81**, 032307 (2010), arXiv:0912.0079.
- [24] H. C. Lim, A. Yoshizawa, H. Tsuchida, and K. Kikuchi, Wavelength-multiplexed entanglement distribution, *Optical Fiber Technology* **16**, 225 (2010).
- [25] S. Wengerowsky, S. K. Joshi, F. Steinlechner, H. Hübel, and R. Ursin, An entanglement-based wavelength-multiplexed quantum communication network, *Nature* **564**, 225 (2018).
- [26] C. Reimer, L. Caspani, M. Clerici, M. Ferrera, M. Kues, M. Peccianti, A. Pasquazi, L. Razzari, B. E. Little, S. T. Chu, D. J. Moss, and R. Morandotti, Integrated frequency comb source of heralded single photons, *Optics Express* **22**, 6535 (2014).
- [27] M. Fujiwara, R. Wakabayashi, M. Sasaki, and M. Takeoka, Wavelength division multiplexed and double-port pumped time-bin entangled photon pair generation using Si ring resonator, *Optics Express* **25**, 3445 (2017).
- [28] M. Förtsch, J. U. Fürst, C. Wittmann, D. Strekalov, A. Aiello, M. V. Chekhova, C. Silberhorn, G. Leuchs, and C. Marquardt, A versatile source of single photons for quantum information processing, *Nature Communications* **4**, 6 (2013).
- [29] X. Guo, C. L. Zou, C. Schuck, H. Jung, R. Cheng, and H. X. Tang, Parametric down-conversion photon-pair source on a nanophotonic chip, *Light: Science and Applications* **6**, 1 (2017).
- [30] L. Caspani, C. Xiong, B. J. Eggleton, D. Bajoni, M. Liscidini, M. Galli, R. Morandotti, and D. J. Moss, Integrated sources of photon quantum states based on nonlinear optics, *Light: Science & Applications* **6**, e17100 (2017).
- [31] B.-S. Shi and A. Tomita, Generation of a pulsed polarization entangled photon pair using a Sagnac interferometer, *Physical Review A* **69**, 013803 (2004).
- [32] T. Kim, M. Fiorentino, and F. N. C. Wong, Phase-stable source of polarization-entangled photons using a polarization Sagnac interferometer, *Physical Review A* **73**, 012316 (2006).
- [33] S. Miki, M. Yabuno, T. Yamashita, and H. Terai, Stable, high-performance operation of a fiber-coupled superconducting nanowire avalanche photon detector, *Optics Express* **25**, 6796 (2017).
- [34] A. Christ, K. Laiho, A. Eckstein, K. N. Cassemiro, and C. Silberhorn, Probing multimode squeezing with correlation functions, *New Journal of Physics* **13**, 033027

- (2011).
- [35] D. F. V. James, P. G. Kwiat, W. J. Munro, and A. G. White, Measurement of qubits, *Physical Review A* **64**, 052312 (2001).
- [36] Z. Y. Ou and Y. J. Lu, Cavity Enhanced Spontaneous Parametric Down-Conversion for the Prolongation of Correlation Time between Conjugate Photons, *Physical Review Letters* **83**, 2556 (1999).
- [37] Y. J. Lu and Z. Y. Ou, Optical parametric oscillator far below threshold: Experiment versus theory, *Physical Review A* **62**, 033804 (2000).
- [38] U. Herzog, M. Scholz, and O. Benson, Theory of biphoton generation in a single-resonant optical parametric oscillator far below threshold, *Physical Review A* **77**, 023826 (2008).
- [39] M. Scholz, L. Koch, and O. Benson, Analytical treatment of spectral properties and signal-idler intensity correlations for a double-resonant optical parametric oscillator far below threshold, *Optics Communications* **282**, 3518 (2009).
- [40] Y. Jeronimo-Moreno, S. Rodriguez-Benavides, and A. B. U'Ren, Theory of cavity-enhanced spontaneous parametric downconversion, *Laser Physics* **20**, 1221 (2010).
- [41] J. A. Zelińska and M. W. Mitchell, Theory of high gain cavity-enhanced spontaneous parametric down-conversion, *Physical Review A - Atomic, Molecular, and Optical Physics* **90**, 1 (2014).
- [42] K.-H. Luo, H. Herrmann, S. Krapick, B. Brecht, R. Ricken, V. Quiring, H. Suche, W. Sohler, and C. Silberhorn, Direct generation of genuine single-longitudinal-mode narrowband photon pairs, *New Journal of Physics* **17**, 073039 (2015).
- [43] O. Slattery, L. Ma, K. Zong, and X. Tang, Background and Review of Cavity-Enhanced Spontaneous Parametric Down-Conversion, *Journal of Research of the National Institute of Standards and Technology* **124**, 124019 (2019).
- [44] Z.-Y. J. Ou, *Multi-photon quantum interference*, Vol. 43 (Springer, 2007).
- [45] C. W. Gardiner and M. J. Collett, Input and output in damped quantum systems: Quantum stochastic differential equations and the master equation, *Physical Review A* **31**, 3761 (1985).
- [46] D. F. Walls and G. J. Milburn, *Quantum optics* (Springer Science & Business Media, 2007).
- [47] J. Garrison and R. Chiao, *Quantum optics* (Oxford University Press, 2008).
- [48] E. Pomarico, B. Sanguinetti, C. I. Osorio, H. Herrmann, and R. T. Thew, Engineering integrated pure narrow-band photon sources, *New Journal of Physics* **14**, 033008 (2012).
- [49] S. Parker, S. Bose, and M. B. Plenio, Entanglement quantification and purification in continuous-variable systems, *Physical Review A* **61**, 032305 (2000).
- [50] C. K. Law, I. A. Walmsley, and J. H. Eberly, Continuous Frequency Entanglement: Effective Finite Hilbert Space and Entropy Control, *Physical Review Letters* **84**, 5304 (2000).
- [51] G. Harder, V. Ansari, B. Brecht, T. Dirmeier, C. Marquardt, and C. Silberhorn, An optimized photon pair source for quantum circuits, *Optics Express* **21**, 13975 (2013).
- [52] X. Shi, K. Guo, J. B. Christensen, M. A. Castaneda, X. Liu, H. Ou, and K. Rottwitt, Multichannel Photon-Pair Generation with Strong and Uniform Spectral Correlation in a Silicon Microring Resonator, *Physical Review Applied* **12**, 1 (2019).
- [53] A. Seri, D. Lago-rivera, A. Lenhard, G. Corrielli, R. Oselame, M. Mazzera, and H. D. Riedmatten, Quantum Storage of Frequency-Multiplexed Heralded Single Photons, *Physical Review Letters* **123**, 80502 (2019).